RESEARCH

A fully human IgG1 antibody targeting connexin 32 extracellular domain blocks CMTX1 hemichannel dysfunction in an in vitro model

Abraham Tettey-Matey[1,9†], Viola Donati[1,2†], Chiara Cimmino[3,10†], Chiara Di Pietro[1†], Damiano Buratto[4†], Mariateresa Panarelli[6], Alberto Reale[6], Arianna Calistri[6], Maria Vittoria Fornaini[6], Ruhong Zhou[4], Guang Yang[7], Francesco Zonta[8*], Daniela Marazziti[1*] and Fabio Mammano[1,5*]

Abstract

Connexins (Cxs) are fundamental in cell–cell communication, functioning as gap junction channels (GJCs) that facilitate solute exchange between adjacent cells and as hemichannels (HCs) that mediate solute exchange between the cytoplasm and the extracellular environment. Mutations in the *GJB1* gene, which encodes Cx32, lead to X-linked Charcot-Marie-Tooth type 1 (CMTX1), a rare hereditary demyelinating disorder of the peripheral nervous system (PNS) without an effective cure or treatment. In Schwann cells, Cx32 HCs are thought to play a role in myelination by enhancing intracellular and intercellular Ca^{2+} signaling, which is crucial for proper PNS myelination. Single-point mutations (p.S85C, p.D178Y, p.F235C) generate pathological Cx32 HCs characterized by increased permeability ("leaky") or excessive activity ("hyperactive").

We investigated the effects of abEC1.1-hIgG1, a fully human immunoglobulin G1 (hIgG1) monoclonal antibody, on wild-type (WT) and mutant Cx32D178Y HCs. Using HeLa DH cells conditionally co-expressing Cx and a genetically encoded Ca^{2+} biosensor (GCaMP6s), we demonstrated that mutant HCs facilitated 58% greater Ca^{2+} uptake in response to elevated extracellular Ca^{2+} concentrations ($[Ca^{2+}]_{ex}$) compared to WT HCs. abEC1.1-hIgG1 dose-dependently inhibited Ca^{2+} uptake, achieving a 50% inhibitory concentration (EC_{50}) of ~ 10 nM for WT HCs and ~ 80 nM for mutant HCs. Additionally, the antibody suppressed DAPI uptake and ATP release. An atomistic computational model revealed that serine 56 (S56) of the antibody interacts with aspartate 178 (D178) of WT Cx32 HCs, contributing to binding affinity. Despite the p.D178Y mutation weakening this interaction, the antibody maintained binding to the mutant HC epitope at sub-micromolar concentrations.

In conclusion, our study shows that abEC1.1-hIgG1 effectively inhibits both WT and mutant Cx32 HCs, highlighting its potential as a therapeutic approach for CMTX1. These findings expand the antibody's applicability for treating

---

[†]Abraham Tettey-Matey, Viola Donati, Chiara Cimmino, Chiara Di Pietro, Damiano Buratto contributed equally to this work.

*Correspondence:
Francesco Zonta
francesco.zonta@xjtlu.edu.cn
Daniela Marazziti
daniela.marazziti@cnr.it
Fabio Mammano
fabio.mammano@unipd.it
Full list of author information is available at the end of the article

Tettey-Matey *et al. Cell Communication and Signaling*   (2024) 22:589

Page 2 of 18

diseases associated with Cx HCs and inform the rational design of next-generation antibodies with enhanced affinity and efficacy against mutant HCs.

Plain English summary

Connexins (Cxs) are proteins essential for communication between cells, forming gap junction channels (GJCs) that connect neighboring cells and hemichannels (HCs) that link the inside of cells to their surroundings. Mutations in the *GJB1* gene, which makes Cx32, cause X-linked Charcot-Marie-Tooth type 1 (CMTX1), a rare nerve disorder that currently has no cure. Our research studied the effects of a specially designed antibody, abEC1.1-hIgG1, on both normal and mutated Cx32 HCs using a well-established cell model for studying these channels. We discovered that the antibody significantly reduced the movement of calcium ions (Ca^{2+}), which are vital for nerve health, in both normal and mutated channels. Further analysis showed that the antibody's success might be due to how it binds to certain areas of the channels. Our findings suggest that abEC1.1-hIgG1 could be developed into a treatment for CMTX1 and similar conditions. Moreover, this research could help in creating even more effective antibodies for targeting faulty hemichannels.

Background

Hereditary demyelinating diseases of the peripheral nervous system (PNS), collectively known as Charcot–Marie–Tooth (CMT) diseases, are rare yet among the most common genetic disorders, affecting approximately 1 in 2500 individuals [1]. Currently, there are no treatments available to cure or slow disease progression [2]. X-linked Charcot-Marie-Tooth disease type 1 (CMT1X, MIM #304040) is a dominant subtype, accounting for about 17% of all CMT cases [3]. Patients typically experience progressive muscle weakness, amyotrophy, and sensory abnormalities, especially in the distal extremities [4–6].

CMT1X arises from over 450 known mutations, including missense, frameshift, deletion, and nonsense mutations in the *GJB1* gene, which encodes the protein connexin (Cx) 32 (Cx32) [7, 8]. Cxs form hexameric membrane structures called connexons or hemichannels (HCs), which dock to form gap junction channels (GJCs) between neighboring cells [9]. GJCs enable direct cytoplasmic communication, while undocked HCs mediate ion and molecule exchange with the extracellular environment [10].

In Schwann cells, Cx32 GJCs are crucial for connecting different layers of the myelin sheath, facilitating the diffusion of ions like K^+ and essential metabolites [11]. As the majority of Cx32 mutations implicated in CMTX1 are loss-of-function [12, 13], the hypothesis is that reduced permeability of mutant GJCs to signaling molecules, such as cyclic adenosine monophosphate (cAMP), disrupts myelin homeostasis and contributes to CMT1X neuropathy [14, 15].

However, CMTX1 is also linked to certain Cx32 gain-of-function mutations (e.g., p.S85C, p.D178Y, and p.F235C) which affect the HCs [16–18]. Cx HCs typically remain closed under physiological conditions, opening transiently only in response to specific stimuli, such as changes in extracellular or cytosolic Ca^{2+} levels [19, 20] to allow the passage of ions and small molecules, influencing cell signaling [21, 22]. ATP released through open HCs can activate purinergic receptors (e.g., P2X and P2Y receptors) on neighboring cells [23, 24], triggering signaling pathways that may promote neuroinflammatory processes [25–27], which can worsen nerve damage and hinder regeneration in hereditary neuropathies [28, 29].

This study evaluates an antibody targeting an extracellular domain shared by Cx26, Cx30, and Cx32 HCs. This antibody has shown nanomolar sensitivity and proven efficacy in inhibiting HCs in previous studies [30–34]. Here, we extend these findings by examining the antibody's effects on Ca^{2+} influx, dye uptake, and ATP release in cells conditionally expressing wild-type (WT) or p.D178Y mutant Cx32, using the genetically encoded Ca^{2+} indicator GCaMP6s [33, 35]. Our results propose this antibody as a promising candidate for treating CMT1X patients with leaky or hyperactive HCs and offer insights for designing improved therapeutic antibodies.

Methods

Viruses

For conditional expression of the Cx of interest and cytosolic GCaMP6s, we followed the methods of Nardin et al. [33] and Tettey-Matey et al. [36]. Briefly, we modified a mammalian expression, lentivirus (LV),

Tet-On [37], destination vector with a puromycin selection marker (pCW57.1, a gift from David Root; Addgene plasmid # 41393; http://n2t.net/addgene:41393; RRID: Addgene_41393; accessed on 01 November 2024). A multiple cloning site (MCS) linked to an Internal Ribosome Entry Site (IRES) and GCaMP6s nucleotide sequences (MCS-IRES-GCaMP6s) was gene-synthesized and inserted between the NheI (GCTAGC) and BamHI (GGATCC) restriction enzyme sites in the pCW57.1 vector to form a new LV transfer vector, which we named pCW57-MSC-IRES-GCaMP6s. Next, the MCS in this vector was used to subclone the coding sequence (CDS) of human Cx32 (*GJB1*, NCBI CCDS ID: CCDS14408.1) or its mutant p.D178Y. We thus obtained two corresponding inducible bicistronic lentiviral plasmids, named pCW57-Cx32-IRES-GCaMP6s [36] and pCW57-Cx32D178Y-IRES-GCaMP6s, respectively, for the simultaneous expression of the Cx of interest and cytosolic GCaMP6s. We deposited these plasmids in Addgene where they have been respectively assigned the following IDs: 216795 and 216796 (https://www.addgene.org/Fabio_Mammano/, accessed on 30 October 2024).

Establishment of inducible cell pools overexpressing the Cx of interest

HeLa DH cells (Merck, 96112022-DNA-5UG) were cultured at 37 °C in a 5% CO_2/95% air atmosphere using complete growth medium obtained by supplementing Dulbecco's Modified Eagle Medium (DMEM, high glucose 4.5 g/L, sodium pyruvate 110 mg/L) with 10% heat-inactivated fetal bovine serum (FBS), 2 mM L-glutamine, and 1% penicillin/streptomycin. The culture medium was replaced every other day.

The pCW57-Cx32-IRES-GCaMP6s and pCW57-Cx32D178Y-IRES-GCaMP6s plasmids were used to produce LV particles by transfecting HEK-293 T cells (American Type Culture Collection, CRL-3216) with Lipofectamine 2000 (Thermo Fisher Scientific, TFS, 11668–027) following a standard protocol [38]. LV-containing supernatant was collected, cleared by filtration, and immediately used to infect HeLa DH cells as detailed in Tettey-Matey et al. [36]. Following puromycin selection of virally transduced HeLa DH cells, the ordinary FBS was replaced with Tetracycline negative FBS collected in South America (Capricorn Scientific, FBS-TET-12B).

qPCR

Total RNA was extracted with TRIzol Reagent (TFS, 15596,018) from HeLa-Cx32-GCaMP6s and HeLa-Cx32D178Y-GCaMP6s cells plated at a density of 2.5×10^5/ml in 35 mm ∅ Petri dishes and exposed or not exposed to doxycycline (dox, 4 μg/ml; Merck, D1822) for 48 h. Ten (10) μg of the extracted total RNA was digested with DNase I (TFS, 18068015) and purified using Rneasy mini Kit (Qiagen, 74104) according to the manufacturer's instructions. A NanoDrop spectrophotometer was used to quantify the RNA by measuring the absorbance. Reverse transcription PCR (RT-PCR) was performed from 1 μg of the purified RNA using a high-capacity cDNA kit (TFS, 4368814), according to the manufacturer's instructions but with a slight modification in which Oligo(dt) (TFS, 18418012) was combined with the cDNA kit random primers at a ratio of 1:5.

qPCR was performed on the cDNA with specific primers (see below). Samples were analyzed at least in triplicate and gene expression levels were estimated by the $2^{-\Delta\Delta CT}$ method [39], using glyceraldehyde-3-phosphate dehydrogenase (GAPDH) as the internal reference gene and SYBR green (SsoAdvanced Universal SYBR green Supermix; BioRad, 1725274) on the ABI 7900HT sequence detection system equipped with the AB1 7900HT SDS software (Applied Biosystems) applying the following amplification cycles: 50 °C, 2 min (1 cycle); 95 °C, 10 min (1 cycle); 95 °C, 15 s; 62 °C, 35 s (40 cycles).

The primers used for these experiments were:

> Cx32 (Cx32 WT and Cx32D178Y): Forward 5′-CGTGAACCGGCATTCTACTG-3′; Reverse 5′-TGGTCATAGCAAACGCTGTTG-3′.
> EMCV-IRES: Forward 5′-AATGTGAGGGCCCGGAAACC-3′; Reverse 5′-ACTCACAACGTGGCACTGGG-3′.
> GCaMP6s: Forward 5′-GGAGGACGGCAACATC-3′; Reverse 5′-GAAAGCCTCTTTAAATTCTGCG-3′.
> GAPDH: Forward 5′-CACCATCTTCCAGGAGCGAG-3′; Reverse 5′-CCTTCTCCATGGTGGTGAAGAC-3′.

Immunofluorescence

HeLa-Cx32-GCaMP6s and HeLa-Cx32D178Y-GCaMP6s cells (1×10^5) were plated onto round glass coverslips (12 mm ∅) in 35 mm ∅ Petri dishes and exposed to dox (4 μg/ml) or vehicle for 48 h. Cells were fixed with 4% paraformaldehyde (PFA; TFS, 047392.9 M) for 15 min, permeabilized with 0.1% Triton X-100 (TFS, A16046.AE) for 5 min and incubated for 1 h in blocking buffer containing 2% bovine serum albumin (BSA; A4503, Merck) and 0.1% Triton X-100. Samples were then incubated overnight at 4 °C with a commercial anti-Cx32 monoclonal antibody (1:200; TFS, 35–8900) diluted in blocking buffer. The next day, samples were washed three times with phosphate buffered saline (PBS; TFS, 10010023) and incubated with Alexa Fluor 555-conjugated Donkey anti-Mouse IgG

Tettey-Matey *et al. Cell Communication and Signaling*   (2024) 22:589

Page 4 of 18

(1:800; TFS, A-31570) or Alexa Fluor 488-conjugated Goat anti-Mouse IgG (1:800; TFS, A-11029) for 1 h at room temperature. For co-immunofluorescent staining of GCaMP6s, samples were then incubated overnight at 4 °C with anti-GFP polyclonal antibody (1:200; TFS, A-11122), which recognizes also GCaMP6s, diluted in blocking buffer. The next day, samples were washed three times with PBS and incubated with Alexa Fluor 488-conjugated Donkey anti-Rabbit IgG (1:800; TFS, A-21206) for 1 h at room temperature. Cell nuclei were stained with 4′,6-diamidino-2-phenylindole (DAPI; TFS, D1306) (5 μg/ml, 5 min) and coverslips were mounted with Pro-Long Gold (TFS, P36934).

For experiments with abEC1.1-hIgG1, we prepared a Ca^{2+}-free medium (ZCM) containing (in mM): 138 NaCl, 5 KCl, 0.4 NaH_2PO_4, 6 D-Glucose, 10 HEPES (all from Merck), pH 7.3. Throughout this article, we refer to ECM as the medium obtained by adding 60 μM $CaCl_2$ to ZCM. Live cells exposed to dox (4 μg/ml) for 48 h, were incubated at 37 °C in ECM supplemented with 10 nM abEC1.1-hIgG1 for 1 h. Next, cells were fixed with 4% PFA for 10 min and incubated for 1 h with Alexa Fluor 594-conjugated Goat anti-Human IgG (1:800; Jackson ImmunoResearch, 109–585-170). Samples were then washed three times with PBS between all steps and Cx32 staining was performed as indicated above. Cell nuclei were stained with DAPI (5 μg/ml, 5 min).

Visualization of plasma membrane was performed using MemBrite Fix 640/660 (Biotium, 30097). Briefly, live cells were incubated with a solution of MemBrite probes for 1 min at 37 °C, according to manufacturer's instruction. After incubation, the excess of MemBrite was washed with HBSS, the cells were fixed, and Cx32 and DAPI staining were performed as indicated above.

Immunofluorescence images were acquired with a TCS SP5 confocal microscope (Leica Microsystems) equipped with a 40×oil immersion objective (Leica Microsystems, HCX PL Apo, UV optimized, N.A. 1.25, oil). Alexa Fluor 488 and GCaMP6s fluorescence was excited by a 488-nm Argon laser and collected between 500 and 540 nm. Alexa Fluor 555 and Alexa Fluor 594 were excited by a 543-nm HeNe laser and collected between 568 and 680 nm and between 600 and 670 nm, respectively.

Immunofluorescence images were also acquired with an FV1200 confocal microscope (Olympus Corporation) equipped with 60×oil immersion objective (Olympus Corporation, PLAPON60XOSC, N.A. 1.40) and visualized with the FV10-ASW software (version 4.2; Olympus Corporation). Confocal through-focus image sequences (z-stacks) were collected with steps of 0.5 μm along the optical axis. DAPI fluorescence was excited by a 405 laser and collected between 425 and 475 nm; Alexa Fluor 488 fluorescence was excited by a 488 laser and

collected between 500 and 545 nm. Alexa Fluor 555 and Alexa Fluor 594 were excited by a 559-nm laser and their emissions were collected between 575 and 620 nm and between 575 and 675 nm, respectively. MemBrite fluorescence was excited by a 635-nm laser and its emission was collected between 655 and 755 nm.

Assay of GCaMP6s functionality
Forty-eight hours after dox induction (4 μg/ml), cell-plated coverslips with a live, confluent cell population were transferred to the previously described spinning disk confocal system [40]. Cells were maintained under the microscope objective at 37 °C in a heated chamber (1.5 ml capacity) and perfused with ZCM, supplemented with either 2 mM or 0.2 mM Ca^{2+}. Sequences of fluorescence images were acquired at 1.5-s intervals using a cooled sCMOS camera (PCO, EDGE; resolution: 2560×2160 pixels, 6.5 μm×6.5 μm, 4×binning).

GCaMP6s was excited using a 488 nm diode laser (Cat. No. COMPACT-150G-488-SM, World Star Tech), and fluorescence emission (*F*) was collected through a 535/30 nm band-pass filter (Cat. No. ET535/30 M, Chroma Technology). Images were analyzed offline using ImageJ and MATLAB (R2019a, The MathWorks). GCaMP6s signals, *F*(*t*), where *t* denotes the time of frame acquisition, were calculated as pixel spatial averages from regions of interest (ROIs) drawn around the perimeter of at least 10 cells per field of view (FOV). To correct for back reflections and electronic offsets, background signals from a cell-free ROI were subtracted [41].

Ca^{2+} uptake
Forty-eight hours after dox induction (4 μg/ml), coverslips were transferred to a heated chamber (1 ml capacity) on an upright SP8-DIVE-STED-FALCON laser scanning confocal fluorescence microscope (Leica Microsystems), equipped with a white laser and a 25×water immersion objective (HC IRAPO, N.A. 1.00). For control experiments, cells were incubated at 37 °C for 15 min in ECM. For pharmacological studies, cells were pre-incubated for 30 min at 37 °C in ECM containing either 100 μM flufenamic acid (FFA; Merck, F9005) or varying concentrations of abEC1.1-hIgG1, ranging from 0.001 nM to 5 μM.

GCaMP6s was excited at 488 nm, and fluorescence emission was spectrally detected between 500 and 535 nm. Sequences of fluorescence images were acquired at 1.3 s intervals for a 6 min period. Following a 10 s baseline recording, a 2 μl bolus of 1 M $CaCl_2$ was delivered at the edge of the field-of-view (FOV) using a 2.5 μm Ø glass capillary connected to a pneumatic pico-pump (SYS-PV830, World Precision Instruments). Three min

Tettey-Matey *et al. Cell Communication and Signaling*   (2024) 22:589

Page 5 of 18

later, 2 µl of 200 µM ionomycin (Merck, I3909) [42] was administered to elicit maximum fluorescence signals.

Image sequences were analyzed offline using Suite2p [43] and MATLAB (R2019a, The MathWorks). GCaMP6s signals were extracted as pixel spatial averages from ROIs drawn around the perimeter of at least 20 cells per FOV. Baseline fluorescence (F_0) traces (one per ROI) were corrected for photobleaching by fitting with an exponential decay function and subtracting this fit from each trace. Each $\Delta F(t)$ trace, defined as $\Delta F(t) = F(t) - F_0$, was normalized to its respective ΔF_{max}, the maximum $\Delta F(t)$ response evoked by ionomycin.

DAPI uptake
Forty-eight hours after dox induction, coverslips with cells were transferred to a spinning disk confocal microscope [40] equipped with a 20×water immersion objective (Olympus, XLUMPlan Fl, N.A. 0.95). For control experiments, cells were pre-incubated for 30 min at 37 °C in ECM, followed by a 5-min incubation with 5 µM DAPI in ECM at room temperature in the dark. For pharmacological experiments, cells were similarly pre-incubated for 30 min at 37 °C in ECM containing either 50 µM FFA or 1 µM abEC1.1-hIgG1, followed by the addition of 5 µM DAPI and a 5-min incubation at room temperature in the dark.

DAPI was excited using a 385 nm LED (M385L3, Thorlabs), and emission was collected through a blue bandpass filter (Semrock, FF01-425/26–25) using a cooled sCMOS camera (PCO, EDGE; resolution 2560×2160 pixels, 6.5 µm×6.5 µm, binning 4). To account for DAPI uptake by dead cells, the first image was subtracted from all subsequent images, and DAPI uptake traces, $F(t)$, were computed as pixel spatial averages from ROIs drawn around the perimeter of at least 40 cell nuclei per FOV. DAPI uptake rates, $dF(t) / dt$, were estimated by fitting each $F(t)$ trace with a straight line through the origin [44, 45].

ATP release
ATP release from HeLa-Cx32D178Y-GCaMP6s cells was measured using a luciferin/luciferase assay (Promega, GA5010, RealTime-Glo™ Extracellular ATP Assay) with a Varioskan LUX plate reader (TFS, VLB000D0). Cells were seeded in 96-well black plates (Corning, 3603) at a density of 2.5×10^4 cells/well. Forty-eight hours after dox induction, the medium was replaced with 75 µl of phosphate-free solution (PFS) containing 138 mM NaCl, 5 mM KCl, 6 mM D-glucose, 10 mM HEPES, 1 mM $MgCl_2$, and 2 mM $CaCl_2$, pH 7.3. Next, 25 µl of 4X ATP assay reagent was added to each well.

Cells were incubated at 37 °C for 30 min with or without inhibitors (1 µM abEC1.1-hIgG1, 100 µM FFA, or 200 µM $LaCl_3$) in PFS. Baseline luminescence readings were recorded every 30 s, with a 1 s exposure per well. ATP release was stimulated by adding 10 µl of 2 µM 4-Br-A23187 (Merck, 100,107) [19], and luminescence measurements continued for additional 10 min. Data were analyzed using MATLAB, and ATP release was quantified as the area under the baseline-subtracted luminescence curve. Non-induced (−dox) cells were used as negative controls.

Molecular dynamics simulations
The model of Cx32 was constructed using the Protein Data Bank (PDB) crystal structure 7ZXN [46]. Missing segments of the cytoplasmic loop were added with MODELLER [47]. The disordered C-terminal region was truncated from residue 220 onward, consistent with previously published models [48], as structural studies indicate that GJCs formed by different connexins exhibit similar structures in the extracellular region [9]. We hypothesize that truncating the C-terminal does not affect the predictive accuracy of our model, given that the extracellular loops, critical for antibody docking, remain unchanged.

The CHARMM-GUI membrane builder was employed to insert the protein into a POPC lipid bilayer and to introduce the p.D178Y mutation in each protomer of the HC. The fragment antigen-binding (Fab) region of the abEC1.1-hIgG1 antibody was modeled using the AlphaFold-collab web server [49]. We used the HAD-DOCK web server to dock the Fab to the Cx32 HC, enforcing interactions between the Fab's Complementarity Determining Regions (CDRs) and the extracellular loops of Cx32. Two top docking configurations were chosen, and molecular dynamics simulation (MDS) were conducted on both the wild-type (Cx32WT) and mutant (Cx32D178Y) systems.

Each system was solvated with TIP3P water, containing Cl^- and K^+ ions at a concentration of ~ 0.15 M to mimic physiological ionic conditions. The total atom count after solvation was approximately 2.5×10^5. We performed energy minimization followed by pre-equilibration simulations in the NVT and NPT ensembles, applying positional restraints on heavy atoms as described previously [50]. Specifically, a 250 ps NVT simulation was conducted with a 1 fs time step, followed by a 1.6 ns NPT equilibration using a 2 fs time step, both with heavy atom restraints. The final production simulation was run for 100 ns.

MDS and energy minimization were performed using GROMACS [51] with the CHARMM36m force field [52]. Long-range electrostatics were handled using the particle mesh Ewald method [53], with a 12 Å cutoff for Lennard–Jones interactions and a switching function starting

Tettey-Matey *et al. Cell Communication and Signaling*   (2024) 22:589

Page 6 of 18

at 10 Å. Temperature was maintained at 310 K using the V-rescale thermostat [54] with a 1 ps coupling constant, and pressure was controlled at 1 bar using the Parrinello-Rahman barostat [55] with a 5 ps coupling constant. The LINCS algorithm was used to constrain hydrogen-containing bonds, allowing a 2 fs integration time step.

Of the two binding models, only one remained stable throughout the simulation period, so the other was excluded from further analysis. We studied the electrostatic properties using APBS [56] and visualized the results with PyMOL (Schrödinger L, DeLano W. PyMOL, 2020. Available from: http://www.pymol.org/pymol). Additional figures were generated with VMD and Python [57].

Free energy calculation

The free energy perturbation (FEP) Hamiltonian replica-exchange (HREX) method was used to quantify the impact of residue 178 on the binding affinity of the abEC1.1 Fab to Cx32. The initial frame for these calculations was selected from the Cx32WT MDS trajectory after the root mean square distance (RMSD) stabilized, around 70 ns. To enhance computational efficiency, the HC was truncated at the start of the transmembrane helices (TMHs), preserving the extracellular region while applying positional restraints to the TMH residues to keep them fixed in space.

The FEP parameter λ was varied from 0 to 1 to simulate the transformation from the wild-type (WT, D178) to the mutant (Y178) state. We used 32 windows with soft-core potentials, each running in parallel. The PMX toolkit [58, 59] was used to parameterize amino acid mutations within the CHARMM36 force field. Simulations were conducted using GROMACS, saving energy values every 10 ps and attempting exchanges between adjacent windows every 2 ps.

We computed the free energy change for both the complex (ΔGcomplex) and the unbound state (ΔGfree) using Alchemical Analysis [60], and then calculated the binding free energy difference ($\Delta\Delta$G) using a thermodynamic cycle approach [61]. To ensure statistical robustness, we performed five independent replicas for the FEP calculations. Each state within each replica was simulated for 48 ns, with 1.5 ns per window, resulting in a cumulative simulation time of 2.88 μs (48 ns × 2 states × 5 replicas × 6 connexins).

Statistics

Statistical analyses were performed using MATLAB (R2019a, The MathWorks). The normality of data distributions was assessed with the Shapiro–Wilk test. For normally distributed data, comparisons of means were conducted using ANOVA, followed by Bonferroni post hoc tests for multiple group comparisons or two-tailed t-tests for comparisons between two groups. For non-normally distributed data, the Kruskal–Wallis test was used, with Dunn-Sidak post hoc tests for multiple group comparisons.

Results are presented as mean values ± standard error of the mean (s.e.m.), unless otherwise specified. Sample sizes (n) for each experimental group are indicated in the figure legends. Statistical significance was defined as p-values (p) less than 0.05 and denoted with asterisks in the figures: *, $p < 0.05$; **, $0.005 < p < 0.05$; ***, $p < 0.0005$.

Results

Expression analyses of Cx32, CX32D178Y and GCaMP6s in virally transduced HeLa DH cells

HeLa DH, a human cervix carcinoma cell line, has been widely used for studying GJC formation, intercellular GJC and HC permeability, and sensitivity to pharmacological modulators [45, 62–67]. These cells are known for their stable membrane potentials, robustness under double whole-cell patch-clamp measurements, and low endogenous expression of Cx45 [68]. Prior studies have shown that the abEC1.1 antibody has minimal effects on Cx45 HCs [31].

In our study, we used qPCR assays to analyze the expression of Cx32, Cx32D178Y, and GCaMP6s in inducible pools of HeLa-Cx32-GCaMP6s and Cx32D178Y-GCaMP6s cells. We chose the Tet-On inducible system [37] for Cx expression [33, 36] because constitutive overexpression of hyperactive or leaky HCs is cytotoxic [69, 70]. Upon the addition of dox (4 μg/ml) to the culture medium, Cx mRNA levels increased over 50-fold within 48 h (Fig. 1a, b). A similar increase was observed for GCaMP6s mRNA (Fig. 1c) and IRES mRNA (Fig. S1). The non-zero expression of these mRNAs in the absence of dox is likely due to the minimal basal leakiness of the tetracycline-responsive element (TRE) promoter in the lentiviral construct [71].

Protein expression was confirmed by immunofluorescence staining using a well-characterized commercial antibody that recognizes an intracellular epitope in the C-terminus of Cx32 in permeabilized cells [72]. The staining revealed fluorescent puncta distributed throughout the cytoplasm and at cell–cell contacts, indicating the presence of intercellular GJCs (Fig. 2a; Fig. S2), consistent with previous observations of Cx32 and its mutants in HeLa cells [73]. To specifically label HCs at the plasma membrane, live cells were treated with the abEC1.1-hIgG1 antibody, followed by fixation and counterstaining with a fluorescent secondary antibody that recognizes the human Fc domain of the antibody (Fig. 2b) [33].
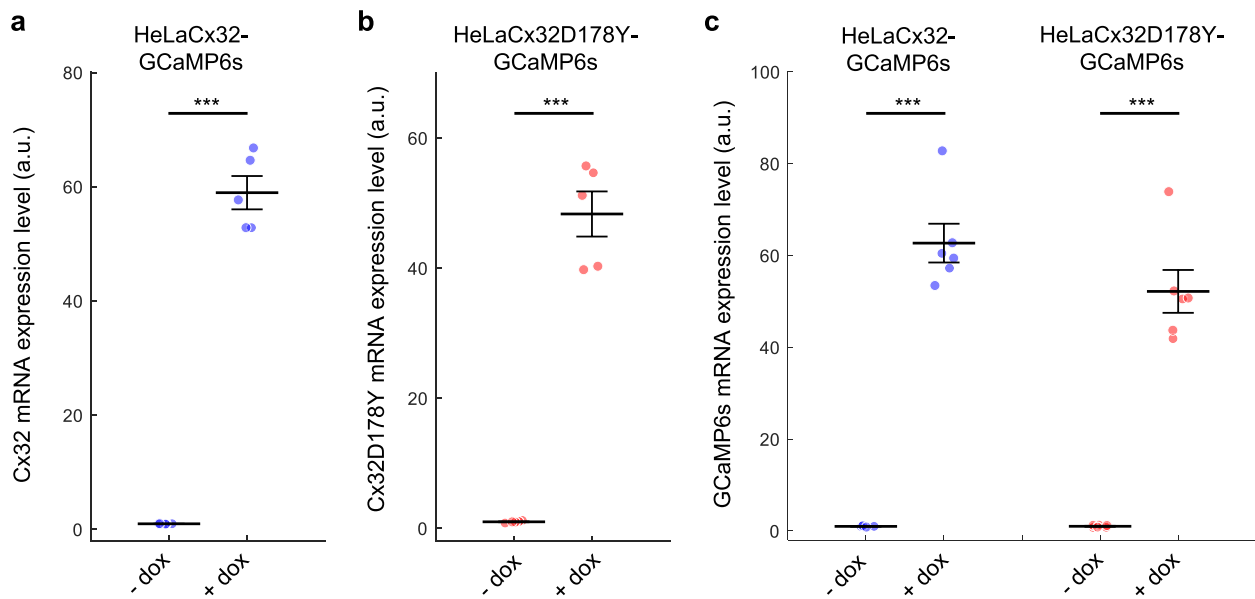
Fig. 1 Validation of Tet-On bicistronic lentiviral vectors. Dot plots showing mean ± s.e.m. of mRNA expression levels measured by qPCR in cells exposed to doxycycline for 48 h (+ dox) or not (− dox): **a** Cx32, **b** Cx32D178Y, and **c** GCaMP6s. Asterisks indicate statistical significance (*p*-value, Kruskal–Wallis (KW) test); *n* > 3 independent cell cultures per condition

Functional assays of the co-expressed Ca²⁺ indicator GCaMP6s

We conducted Ca^{2+} imaging experiments to confirm the functionality of the co-expressed GCaMP6s indicator (Fig. 3 and Video S1). When cells were maintained in a solution containing 2 mM extracellular Ca^{2+} ($[Ca^{2+}]_{ex}$), Cx HCs remained mostly closed [20], resulting in only brief, low-amplitude fluctuation of the GCaMP6s fluorescence signal, $F(t)$, attributed to spontaneous cytosolic Ca^{2+} ($[Ca^{2+}]_{cyt}$) oscillations (Fig. 3a, b) [74]. The amplitudes and inter-peak intervals of these oscillations displayed non-normal frequency distributions (Fig. S3).

Lowering $[Ca^{2+}]_{ex}$ to 0.2 mM halted the $[Ca^{2+}]_{cyt}$ oscillations within 3 min (Fig. 3c) and opened the HCs [20]. The rapid reintroduction of 2 mM $[Ca^{2+}]_{ex}$ triggered a substantial Ca^{2+} influx through the open HCs [33, 75], resulting in pronounced, longer-duration $[Ca^{2+}]_{cyt}$ transients (Fig. 3c). The mean amplitude and full width at half maximum (FWHM) of these transients were both 9-fold higher, compared to those of the spontaneous $[Ca^{2+}]_{cyt}$ oscillations (Fig. 3d, e). These experiments confirmed two key points: (i) GCaMP6s expressed after dox induction effectively reports $[Ca^{2+}]_{cyt}$ fluctuations and (ii) the $[Ca^{2+}]_{cyt}$ transients induced by the reintroduction of 2 mM $[Ca^{2+}]_{ex}$ are readily distinguishable from the baseline oscillations observed under normal $[Ca^{2+}]_{ex}$ conditions.

Effect abEC1.1-hIgG1 on Ca²⁺ uptake

Given the role of deregulated Ca^{2+} signaling in the pathogenesis of CMTX1 [17, 76], we quantified Ca^{2+} uptake through open HCs (Fig. 4 and Video S2-S5) [33, 75]. Pre-incubation with 100 μM FFA, a common Cx channel inhibitor [77], significantly reduced the cytosolic Ca^{2+} load (CCL), measured as the area under the $\Delta F(t)$ curve of GCaMP6s, in both HeLa-Cx32-GCaMP6s and HeLa-Cx32D178Y-GCaMP6s cells (Fig. 4a-f), and this inhibitory effect was reversible (Fig. S4). These experiments confirmed that Ca^{2+} uptake predominantly involved overexpressed HCs. Notably, the CCL in HeLa-Cx32D178Y-GCaMP6s cells was 58% higher than in HeLa-Cx32-GCaMP6s cells ($p = 1.3 \times 10^{-6}$, KW test), consistent with the notion that the p.D178Y mutation leads to deregulated Ca^{2+} handling by HCs [17].

Next, we evaluated the effect of abEC1.1-hIgG1 on Ca^{2+} uptake (Fig. 4g, h). In HeLa-Cx32-GCaMP6s cells, the antibody began inhibiting Ca^{2+} uptake at 100 pM, with a half-maximal inhibitory concentration (EC_{50}) around 10 nM and maximal inhibition achieved at concentrations above 1 μM. In HeLa-Cx32D178Y-GCaMP6s cells, the antibody remained ineffective at concentrations up to 100 pM, showed an EC_{50} around 80 nM, and reached maximal inhibition at concentrations above 5 μM (Fig. 4h).
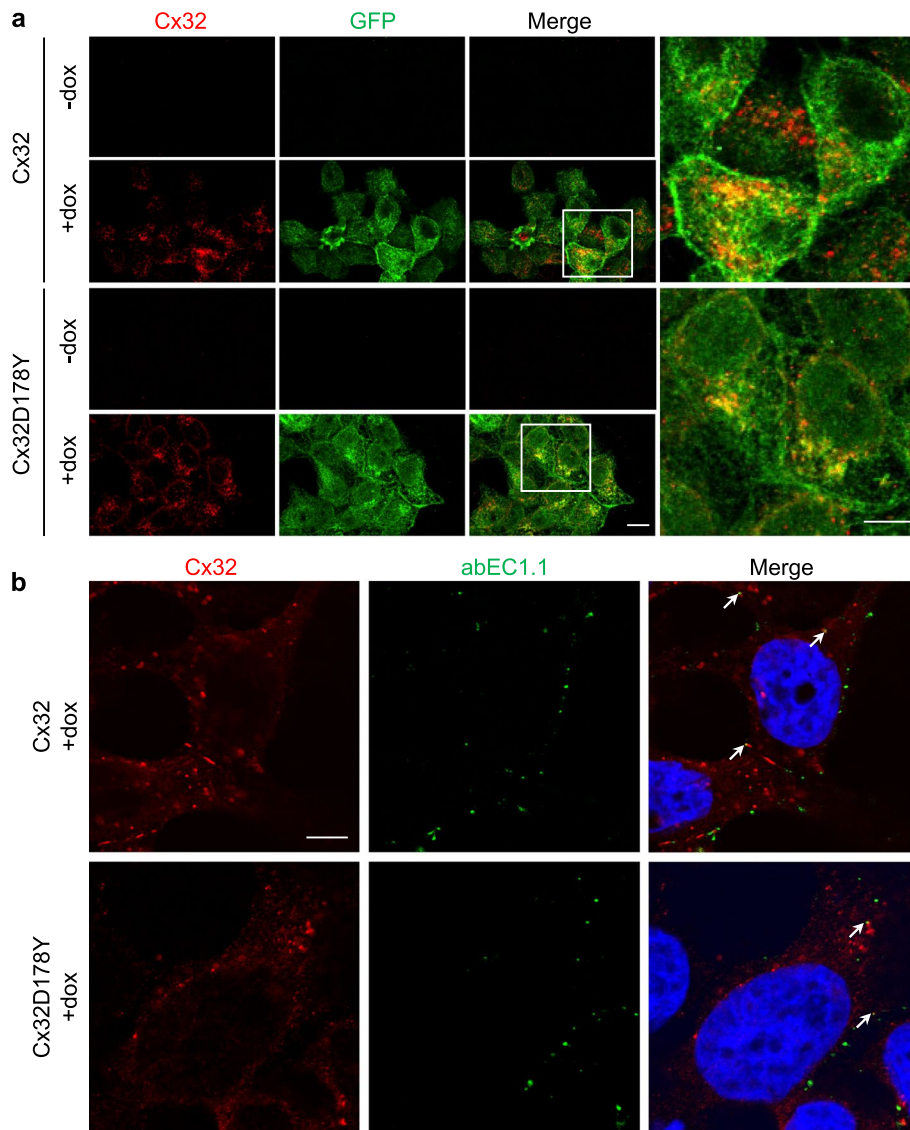
Fig. 2 Immunofluorescence characterization of Cx expression. **a** Representative confocal images of fixed and permeabilized cells expressing human WT Cx32 (upper panels) or mutant Cx32D178Y (lower panels), either exposed to doxycycline for 48 h (+dox) or not exposed (−dox). Cells were labeled with anti-Cx32 (red) and anti-GFP (green) antibodies (the GFP epitope recognized by the antibody is also present in GCaMP6s). Scale bar: 10 µm. Right panels: higher magnification of boxed areas, showing fluorescent puncta at cell–cell contacts; scale bar: 10 µm. **b** Representative confocal images showing immunofluorescence labeling with abEC1.1 and anti-Cx32. Live cells expressing human WT Cx32 (upper panels) or mutant Cx32D178Y (lower panels), exposed to doxycycline for 48 h (+dox), were treated with 10 nM abEC1.1 antibody. Cells were then fixed (but not permeabilized) and counterstained with a secondary antibody selective for the human Fc domain of IgG (green). After permeabilization, cells were stained with anti-Cx32 (red) and counterstained with DAPI (blue) to visualize nuclei. Scale bar: 5 µm

Effect abEC1.1-hIgG1 on DAPI uptake and ATP release

To further validate our observations, we performed DAPI uptake experiments, a widely used method to assess Cx HC activity under various conditions [44, 45]. DAPI is a small fluorescent molecule (277 Da) that can permeate most Cx channels and fluoresces intensely upon binding to A-T-rich regions of nuclear DNA, significantly enhancing its quantum yield [78]. Previous studies have

shown that DAPI uptake in Cx-expressing HeLa cells is more than 10 times faster compared to parental HeLa cells, with uptake rates correlating closely with HC density [65, 79, 80].

In our current experiments, we observed that DAPI uptake in HeLa-Cx32D178Y-GCaMP6s cells, induced with dox for 48 h, was not influenced by changes in $[Ca^{2+}]_{ex}$. However, a 30 min pre-incubation with either
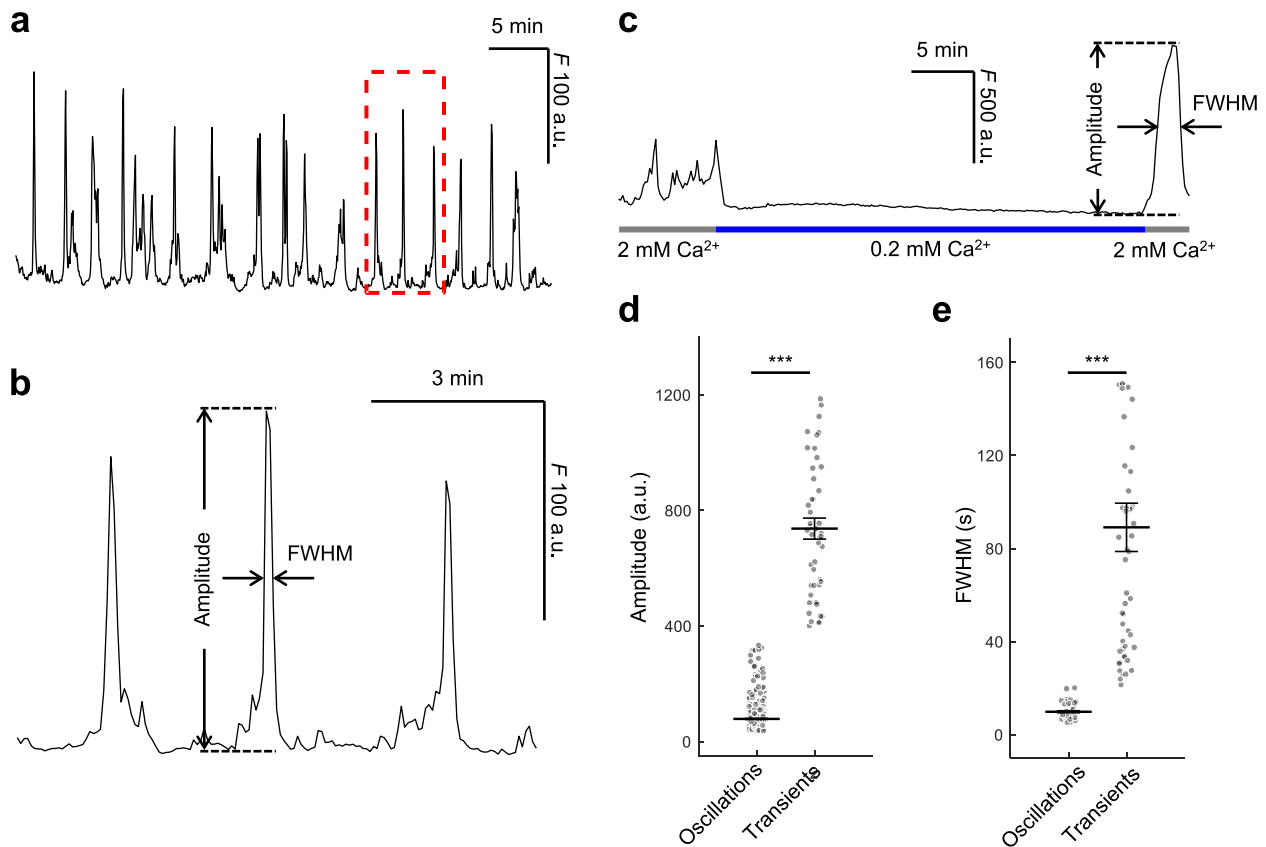
Fig. 3 Functional characterization of GCaMP6s expression. **a** Representative trace of GCaMP6s fluorescence (*F*) emission from HeLa-Cx32-GCaMP6s cells during spontaneous $[Ca^{2+}]_{cyt}$ oscillations in 2 mM extracellular Ca^{2+} ($[Ca^{2+}]_{ex}$). **b** Detail of the oscillations highlighted by the dashed red box in (a) with indication of the parameters used for quantitative data analysis. **c** Effect of reducing $[Ca^{2+}]_{ex}$ from 2 mM to 0.2 mM, followed by a return to 2 mM. **d**, **e** Dot plots with mean ± s.e.m. of amplitude (d) and full width at half maximum (FWHM) (e) of spontaneous $[Ca^{2+}]_{cyt}$ oscillations in 2 mM $[Ca^{2+}]$ex (left) and $[Ca^{2+}]_{cyt}$ transients evoked by increasing $[Ca^{2+}]_{ex}$ from 0.2 mM to 2 mM (right). Asterisks indicate statistical significance (*p*-value, Kruskal–Wallis test); *n* = 40 to 60 cells per condition, 5 independent experiments

(See figure on next page.)

Fig. 4 Ca^{2+} uptake through Cx32 and Cx32D178Y HCs. **a**, **c** Mean GCaMP6s $\Delta F/\Delta F_{max}$ traces (thick lines) in response to a Ca^{2+} stimulus, overlaid with individual cell responses (light lines) from doxycycline-induced HeLa-Cx32-GCaMP6s (**a**) or HeLa-Cx32D178Y-GCaMP6s (**c**) cell cultures. Cells were maintained in ECM (Control, upper panels; *n* > 140 cells) or ECM containing 100 μM FFA (lower panels; *n* > 260 cells). **b**, **d** Dot plots showing cytosolic Ca^{2+} load (CCL), measured as the area under $\Delta F/\Delta F_{max}$ traces from *t* = 0 to *t* = 100 s, with mean ± s.e.m. superimposed. **e**, **f** Representative sequences of fluorescence images taken at the indicated time points (corresponding to the x-axis in panels **a** and **c**, from Video S2-S5); scale bar: 100 μm. **g** Mean GCaMP6s $\Delta F/\Delta F_{max}$ traces (thick lines) overlaid with individual cell responses (light lines) from doxycycline-induced HeLa-Cx32-GCaMP6s (left panels, blue) and HeLa-Cx32D178Y-GCaMP6s (right panels, red) cell cultures in ECM supplemented with increasing concentrations of abEC1.1-hIgG1. **h** Dose-dependent effect of abEC1.1-hIgG1 on the CCL induced by Ca^{2+} uptake through Cx32 HCs (blue squares) and Cx32D178Y HCs (red triangles), based on traces in (**g**). Data are presented as mean ± s.e.m. Asterisks indicate statistical significance (*p*-value, Kruskal–Wallis test); *n* > 15 cells per condition

50 μM FFA or 1 μM abEC1.1-hIgG1 significantly reduced the DAPI uptake rate (Fig. 5). These results further support the hypothesis that (i) the p.D178Y mutation disrupts the normal Ca^{2+} regulation of Cx32 HC activity [17], and (ii) the abEC1.1 blocks Cx32D178Y mutant HCs.

Finally, we also examined ATP release, a key factor in CMTX1 pathogenesis, where aberrant HC activity contributes to disrupted cellular homeostasis [76]. In Cx32-expressing cells, ATP release can be triggered by transient increases in $[Ca^{2+}]_{cyt}$, such as with 4-Br-A23187 at concentrations of 1.5–2 μM [19]. Previous studies demonstrated that abEC1.1 inhibits ATP
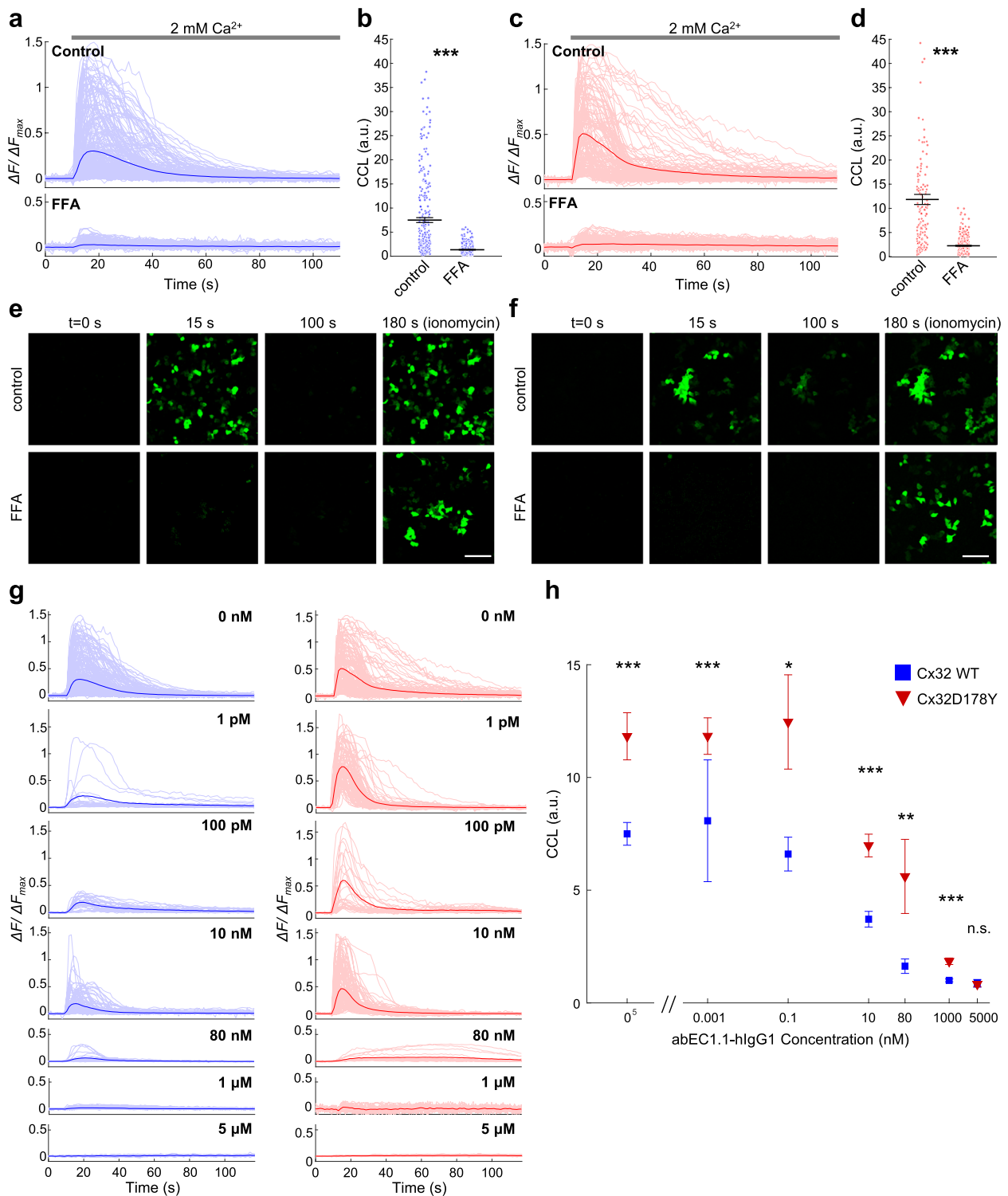
Tettey-Matey *et al. Cell Communication and Signaling*   (2024) 22:589

Page 10 of 18

Fig. 4 (See legend on previous page.)

release from mutant Cx30 HCs linked to Clouston syndrome [32]. Here, we used bioluminescence measurements with a luciferin-luciferase kit to monitor ATP

release from Cx32D178Y HCs in a 96-well plate format at 37 °C (Fig. 6). Non-induced (−dox) cells exhibited minimal ATP release, while dox-induced cells showed
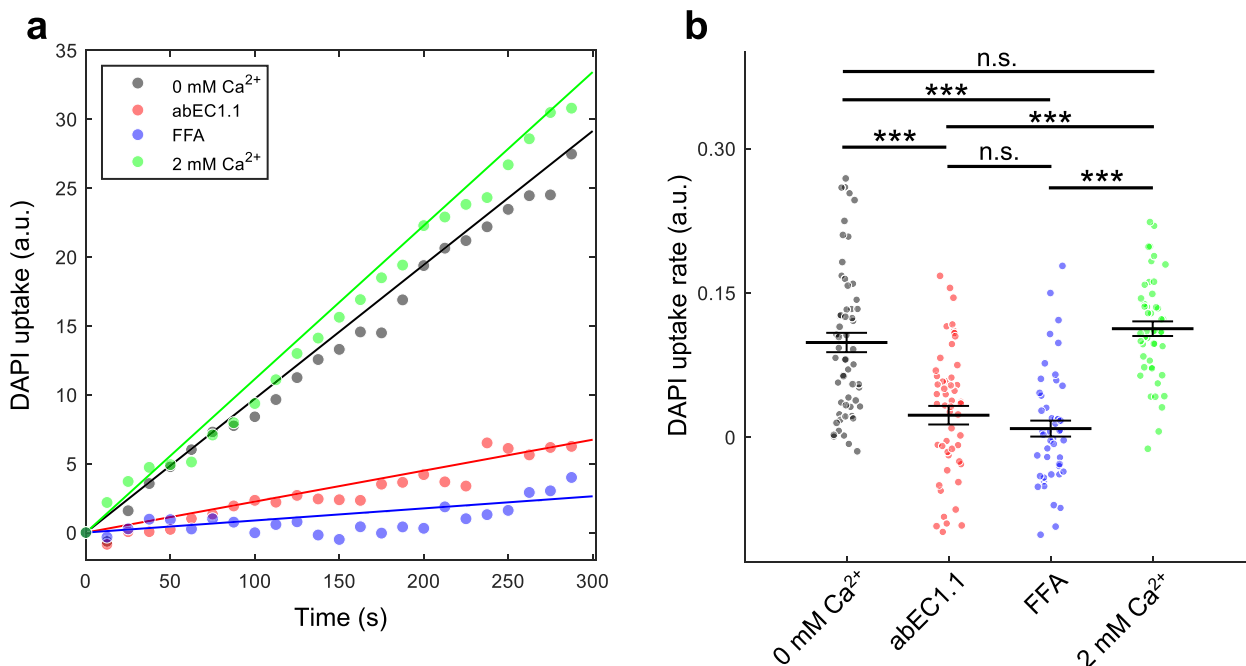
Fig. 5 DAPI uptake through Cx32D178Y HCs. **a** Kinetics of DAPI uptake 48 h post-dox induction. The plots represent the time course of the mean fluorescence intensity from ROIs encompassing the nuclei of $n = 40$ to 60 cells per condition, with data fitted using a least-squares linear regression through the origin. Experiments were performed in 0 Ca^{2+} ZCM, with 1 µM abEC1.1-hIgG1 or 50 µM FFA added as indicated. **b** Dot plots showing DAPI uptake rates, with mean ± s.e.m. superimposed. Asterisks indicate statistical significance (*p*-value, Kruskal–Wallis test); $n = 40$ to 60 cells per condition
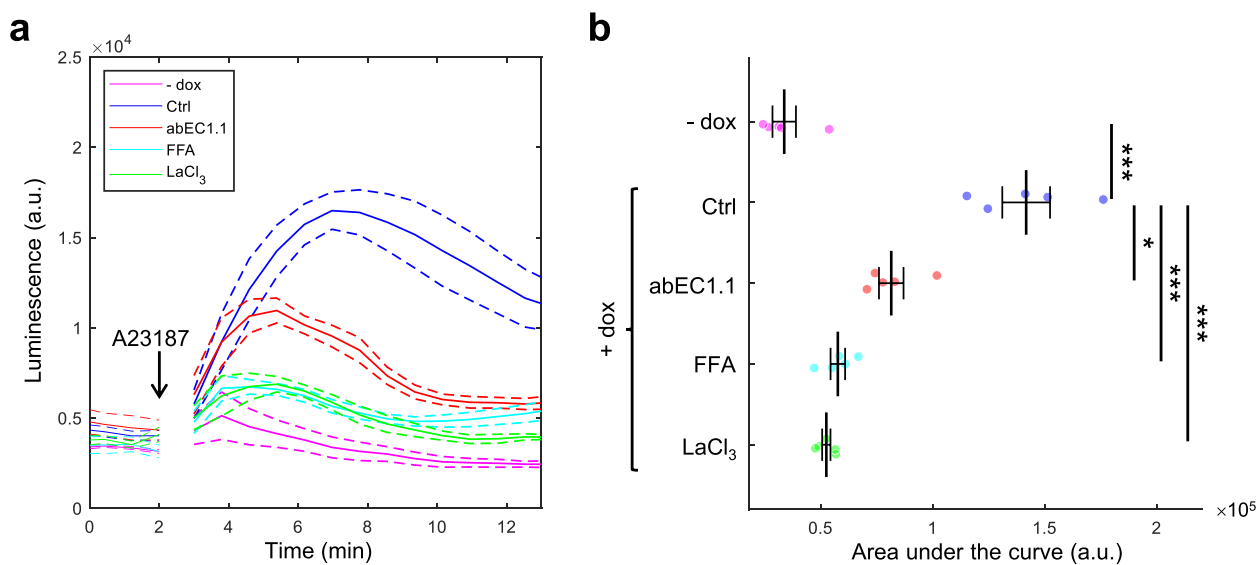
Fig. 6 ATP release through Cx32D178Y HCs. **a** Kinetics of ATP release, shown as mean luminescence signals (solid lines) ± s.e.m. (dashed lines) over time. Gaps in the data following the addition of 2 µM 4-Br-A23187 are due to instrumentation limitations. **b** Dot plots representing the quantification of luminescence data from panel (**a**), with mean ± s.e.m. superimposed. Asterisks indicate statistical significance (*p*-value, ANOVA test); $n = 5$ cell cultures per condition

a robust ATP release response, peaking within 5 min of 2 µM 4-Br-A23187 stimulation, at levels 4-fold higher than baseline (Fig. 6a). The ATP release was significantly inhibited by abEC1.1-hIgG1, FFA, and lanthanum chloride ($LaCl_3$), a non-specific HC blocker [44, 81]. A
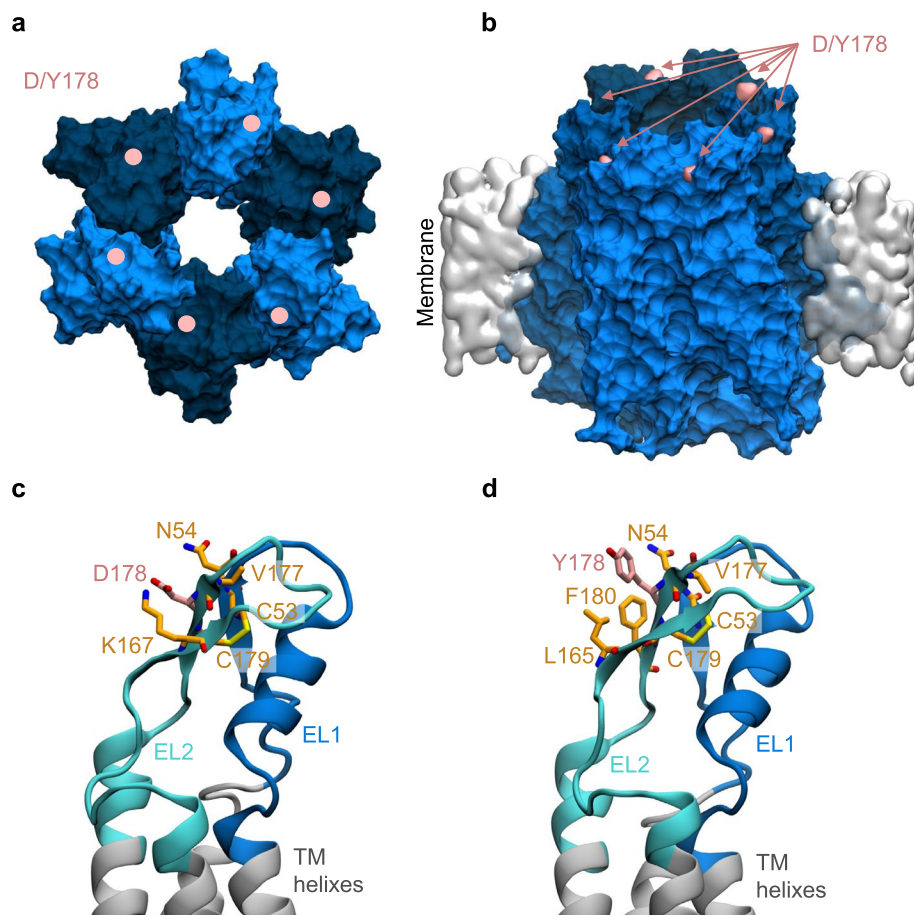
Fig. 7 Atomistic models of WT and D178Y mutant Cx32 HCs. **a** Top view of a Cx32 HC from the extracellular perspective, rendered in surface mode. The six connexin subunits are shown in alternating dark and light blue. The positions of the D/Y178 residues in each connexin are indicated by pink dots. **b** Side view of a Cx32 HC embedded in the lipid membrane, with D/Y178 residues highlighted in pink. **c, d** Close-up views of the residues interacting with D178 (**c**) and Y178 (**d**) within a connexin. Both panels depict the extracellular loops (EL1, EL2) and parts of the transmembrane (TM) helices, showing residues within 3 Å of D/Y178. D/Y178 residues are colored in pink, while the surrounding interacting residues are shown in orange

statistical comparison of the area under the ATP release curve is shown in Fig. 6b.

Modeling abEC1.1-hIgG1 interaction with Cx32 and Cx32D178Y HCs

Previous studies demonstrated that other gain-of-function mutations in Cx HCs, such as Cx30 p.A88V, Cx26 p.G45E and Cx26 p.D50N, did not impact the efficacy of the abEC1.1 antibody when administered in a single-chain format (scFv-Fc) [30, 32, 34]. These mutations are located within the central pore of the HC and are distant from the epitope targeted by the antibody [31]. In contrast, our Ca^{2+} uptake experiments suggested that the p.D178Y mutation, located in the second extracellular loop of Cx32, reduces the affinity of the antibody for Cx32 HCs. This reduction in affinity may be due to the involvement of residue D178 in the interaction with the antibody [31].

To explore this hypothesis and understand the inhibitory mechanism of the antibody, we constructed a structural model of the Cx32 HC (Fig. 7 and Fig. S5) bound to the Fab region of abEC1.1-hIgG1, following methods used previously for modeling abEC1.1(scFv-Fc) [30]. Docking simulations using the HADDOCK web server generated multiple binding modes, which were generally consistent with one another. Among the top-scoring configurations, we selected a model closely resembling the binding of abEC1.1_scFv-Fc to Cx26 (Fig. 8). The stability of this binding mode was tested using a 100 ns MDS, and the results were compared with a parallel simulation in which all six D178 residues were mutated to tyrosine (Y).

The final conformations of the WT and mutant HC-Fab complexes were highly similar (Fig. 8a, b). Both systems equilibrated within 30 ns, and the RMSD from the initial structure stabilized around 3.5 Å. A second docking model was evaluated but produced unstable trajectories
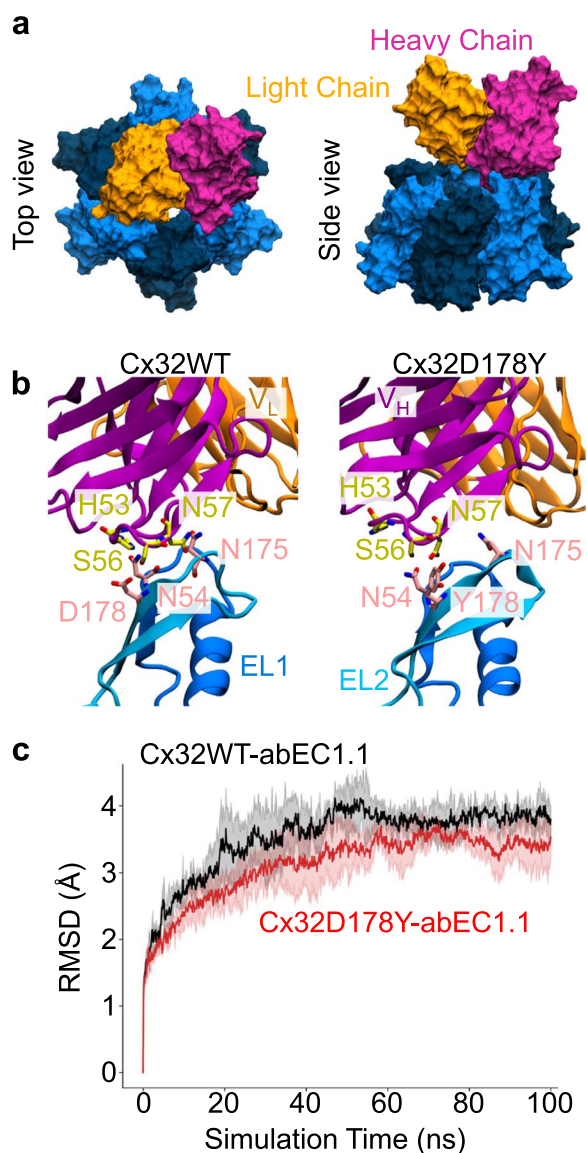
Fig. 8 Model of abEC1.1-hIgG1 Fab bound to WT or mutant Cx32 HC. **a** Final configuration of the HC-Fab complex after 100 ns of MDS, shown from the extracellular view (top) and side view (bottom). Proteins are rendered in surface mode, with connexins depicted in alternating dark and light blue, and the Fab heavy chain and light chain colored in pink and orange, respectively. For clarity, only the extracellular loops and portions of the transmembrane (TM) helices are shown for the HCs. **b** Close-up of the interaction between the D/Y178 residue and the Fab. Only one of the six D/Y178 residues directly interacts with the S56 residue of the Fab. Proteins are displayed in cartoon representation. **c** Comparison of the RMSD during the MDS for the WT and D178Y complexes. Results are presented as the mean (solid line) with standard deviation (shaded area) from three independent replicas

during the 100 ns MDS (Fig. S6) and was therefore discarded.

To quantify the impact of the p.D178Y mutation, we analyzed the percentage of time key amino acids in the HC were in close contact (< 3 Å) with the Fab residues throughout the MDS. Data analysis revealed that only one of the six D178 residues maintained a stable interaction (97% of the simulation time) with serine 56 (S56) on the Fab. The other D178 residues contributed minimally to the interaction. A detailed interaction analysis (Table S1 and S2) indicated that the mutation from aspartate to tyrosine at position 178 significantly reduced contact frequency with the antibody. Specifically, the interaction rate of residue 178 with the antibody decreased from 79% in the WT to just 19% in the mutant.

In silico estimate of binding affinity between abEC1.1 Fab and Cx32 or Cx32D178Y HCs

Analyzing the MDS trajectory alone is often insufficient to fully understand the impact of mutations on the binding affinity between an antibody and its target [82]. Even though molecular simulations can track atomic positions throughout the simulation, they may not clearly reveal the true energetic effects of a mutation. To address this, we performed a direct calculation of the contribution of the residue at position 178 to the binding energy of the Cx32 HC-Fab complex using the Free Energy Perturbation method with Hamiltonian Replica Exchange (FEP-HREX) to improve convergence [83]. The FEP method is a well-established approach for accurately estimating relative binding affinities in diverse chemical and biological systems, including antigen–antibody interactions [84].

In our model, only one of the six D178 residues maintains close contact with the Fab. However, we considered the possibility that the p.D178Y mutation might also indirectly influence the local structure of the extracellular loops, affecting antibody binding. To test this, we mutated each of the six D178 residues individually to tyrosine (Y) and calculated their respective contributions to the overall change in binding affinity using FEP (Fig. 9a, b).

Our results showed that the D178 residue in direct contact with the antibody accounted for the largest change in binding free energy, causing a ΔΔG increase of approximately 1.43 kcal/mol (cyan bar in Fig. 9c). Mutations at two neighboring Cx protomers produced smaller effects, with ΔΔG values of 0.50 kcal/mol and -0.37 kcal/mol (gray and yellow bars in Fig. 9c), even though these residues did not directly interact with the Fab. This suggests that the mutations subtly altered the arrangement of nearby amino acids involved in binding. The remaining three Cx protomers showed no significant contributions to the Fab docking.
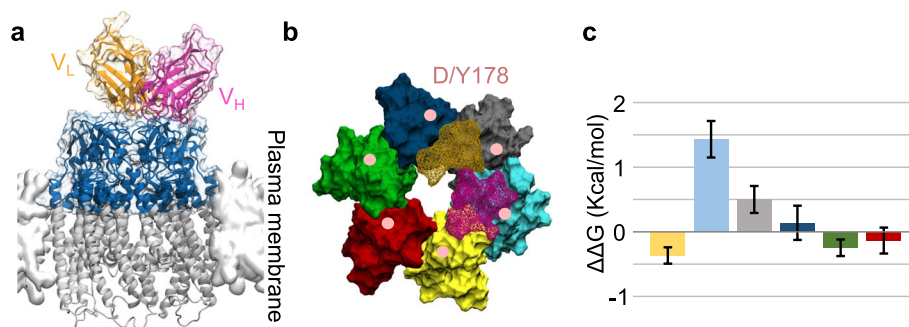
Fig. 9 Binding energy difference (ΔΔG) induced by the p.D178Y mutation. **a** Side view of the Cx32 HC bound to the Fab region of abEC1.1-hIgG1. Only the colored portion of the HC was used for FEP calculations. The Fab's heavy chain and light chain are shown in purple and orange, respectively (VL = light chain variable domain, VH = heavy chain variable domain). **b** Top view of the HC model. The HC is displayed in surface mode, with each Cx protomer rendered in a different color. Fab residues that interact with the HC (within a distance of < 4 Å) are depicted in wire-frame surface mode, with the heavy chain in purple and the light chain in orange. Pink dots mark the location of the D178Y mutation. **c** Binding energy differences (ΔΔG) resulting from the p.D178Y mutation for each Cx protomer, presented as mean ± s.e.m. The color of each bar corresponds to the respective connexin protomer colors shown in panel **b**

Since the residues at position 178 on different Cx protomers do not interact with each other, the overall binding energy difference can be estimated by summing the individual contributions. The total ΔΔG was calculated to be 1.32 kcal/mol, corresponding to an approximate 10-fold decrease in binding affinity. This result is in excellent agreement with our experimental observations.

Discussion

Our study demonstrates that abEC1.1-hIgG1 effectively inhibits Ca^{2+} influx, DAPI uptake and ATP release through mutant Cx32D178Y HCs implicated in CMTX1. Importantly, our data reveal that while the p.D178Y mutation reduces the antibody's affinity, it does not eliminate its inhibitory effect, suggesting that even challenging mutations can be targeted with substantial efficacy.

One of the most compelling aspects of our findings is the mechanistic insight into how the antibody interacts with mutant HCs. MDS and in silico binding studies revealed that the substitution of aspartic acid with tyrosine at position 178 disrupts a critical interaction with the S56 residue of the antibody's Fab region. This disruption affects both the electrostatic and steric properties at the binding interface, providing a molecular explanation for the observed reduction in antibody affinity. However, the overall structural integrity of the extracellular loops allows the antibody to maintain a meaningful level of inhibition.

These observations emphasize the importance of understanding specific residue interactions, suggesting therapeutic potential also for other leaky of hyperactive Cx32 mutants, such as p.S85C and p.F235C, implicated in CMTX1 pathogenesis. Since these mutations are located far from the extracellular antibody-binding domain, the antibody would likely inhibit these mutants similarly, without interference, potentially expanding its therapeutic application across multiple CMTX1 genotypes. This hypothesis is supported by earlier studies of other gain-of-function mutations in Cx HCs far from the antibody's target epitope (such as Cx26 p.G45E, Cx26 p.D50N and Cx30 p.A88V), which did not alter the antibody's effectiveness [30, 32, 35]. Prior work from our lab and others has shown that Cx-targeting antibodies can restore cellular homeostasis by mitigating HC overactivity in mouse models of Keratitis-Ichthyosis-Deafness (KID) syndrome and Clouston syndrome [32, 34, 85]. The pathological mechanisms in HC-related conditions often share similarities [70], suggesting that therapeutic strategies like abEC1.1-hIgG1 could have broader applications [86]. These preclinical successes underscore the potential of HC-specific antibodies to address the root causes of hereditary diseases characterized by connexin dysfunction.

Nevertheless, we must acknowledge the limitations of our study. First, our work relies heavily on in vitro assays. Although these experiments are highly informative and controlled, they do not fully capture the complexity of peripheral nervous system (PNS) pathology in CMTX1. The absence of in vivo data is a significant limitation that must be addressed in future research. Animal models of CMTX1, such as transgenic mice expressing human Cx32 mutations [87, 88], will be essential for assessing the antibody's efficacy under physiological conditions.

Furthermore, our use of truncated Cx32 models for computational studies, while necessary for simplification, may overlook interactions involving the full-length protein, including the cytoplasmic domains that are absent in our simulations. Advances in artificial intelligence (AI)

leveraging the groundbreaking work of 2024 Nobel laureates Demis Hassabis and John Jumper can now accelerate antibody development [89]. These technologies will almost certainly expedite the creation of antibodies tailored to target hyperactive HCs while minimizing off-target effects [90].

Our study also opens avenues for exploring combination therapies. Treatments such as adeno-associated virus (AAV)-mediated antibody gene delivery [34] with novel capsid variants targeting the CNS and PNS [91] could offer a comprehensive approach to CMTX1 management [92]. Given the genetic heterogeneity of CMTX1 and related neuropathies, such a multifaceted approach could provide personalized and durable therapeutic outcomes. However, this therapeutic strategy would require extensive preclinical validation to ensure safety and efficacy. As the International Mouse Phenotyping Consortium (IMPC) continues to develop a broader allelic series for Cx mutations [93], testing abEC1.1-hIgG1 and other rationally designed antibodies across these models will be crucial for establishing their efficacy against a range of CMTX1 variants.

Conclusion

Our study underscores the therapeutic potential of abEC1.1-hIgG1 for treating CMTX1 by effectively reducing aberrant Ca^{2+} influx and ATP release through hyperactive Cx32 HCs. The antibody's demonstrated efficacy against both wild-type and mutant Cx32 HCs indicates its broader applicability for multiple CMTX1 variants and related hereditary neuropathies. Moreover, our findings highlight the promise of antibodies as targeted interventions that address the underlying molecular mechanisms of hereditary diseases caused by Cx mutations [86]. This is further supported by the successful preclinical use of abEC1.1 in managing pathological HC activity in conditions such as KID and Clouston syndromes [32, 34, 85]. As antibody engineering and delivery technologies continue to advance, abEC1.1-hIgG1 represents a significant step toward developing effective, mutation-specific therapies for a range of hereditary disorders linked to connexin dysfunction.

Abbreviations

AAV	Adeno-associated virus
ATP	Adenosine triphosphate
cAMP	Cyclic adenosine monophosphate
Ca^{2+}	Ionized calcium
$[Ca^{2+}]_{cyt}$	Cytosolic free Ca^{2+} concentration
$[Ca^{2+}]_{ex}$	Extracellular free Ca^{2+} concentration
CCL	Cytosolic Ca^{2+} load (area under the curve)
CDR	Complementarity determining region
CDS	Coding sequence
CMT	Charcot–Marie–Tooth
CMTX1	X-linked Charcot Marie Tooth type 1
CNS	Central nervous system
Cx	Connexin
DAPI	4′,6-Diamidino-2-phenylindole
ECM	Extracellular medium containing 60 μM Ca^{2+}
Fab	(Antibody) fragment antigen-binding (region)
FEP	Free energy perturbation
FFA	Flufenamic acid
GJC	Gap junction channel
HC	Hemichannel
HREX	Hamiltonian replica-exchange
IRES	Internal Ribosome Entry Site
hIgG1	Human immunoglobulin G1
IMPC	International Mouse Phenotyping Consortium
MCS	Multiple cloning site
MDS	Molecular dynamics simulation
n	Sample size
p	*p*-Value
PDB	Protein data bank
PFS	Phosphate-free solution
PNS	Peripheral nervous system
RMSD	Root mean square distance
scFv-Fc	Single chain fragment variable-fragment crystallizable (antibody format)
s.e.m.	Standard error of the mean
TMH	Transmembrane helix
TRE	Tetracyclin responsive element
WT	Wild type
ZCM	Extracellular medium containing 0 mM Ca^{2+} (also known as Ca^{2+}-free medium)

Supplementary Information

The online version contains supplementary material available at https://doi.org/10.1186/s12964-024-01969-0.

Additional file 1.

Data availability
No datasets were generated or analysed during the current study.

Declarations

Ethics approval and consent to participate
Not applicable.

Consent for publication
This study does not contain any individual participant data. No consent to publish is required.

Author details

[1]CNR Institute of Biochemistry and Cell Biology, Monterotondo, Rome 00015, Italy. [2]Department of Biomedical Sciences, University of Padua, Padua 35131, Italy. [3]CNR Institute of Endocrinology and Experimental Oncology "G. Salvatore", Naples 80131, Italy. [4]Institute of Quantitative Biology, College of Life Science, Zhejiang University, Hangzhou, Zhejiang 310058, P. R. China. [5]Department of Physics and Astronomy "G. Galilei", University of Padua, Padua 35131, Italy. [6]Department of Molecular Medicine, University of Padua, Padua 35131, Italy. [7]Shanghai Institute for Advanced Immunochemical Studies, ShanghaiTech University, Shanghai 201210, P. R. China. [8]Department of Biological Sciences, School of Science, Xi'an Jiaotong-Liverpool University, Suzhou 215123, P. R. China. [9]Present Address, CNR Institute of Biophysics, Genoa 16149, Italy. [10]Present Address: Interdisciplinary Research Centre On Biomaterials, University of Naples Federico II, Naples 80125, Italy.

References

1. Fridman V, Saporta MA. Mechanisms and treatments in demyelinating CMT. Neurotherapeutics. 2021;18:2236–68.
2. Hertzog N, Jacob C. Mechanisms and treatment strategies of demyelinating and dysmyelinating Charcot-Marie-Tooth disease. Neural Regen Res. 2023;18:1931–9.
3. Panosyan FB, Laura M, Rossor AM, Pisciotta C, Piscosquito G, Burns J, Li J, Yum SW, Lewis RA, Day J, et al. Cross-sectional analysis of a large cohort with X-linked Charcot-Marie-Tooth disease (CMTX1). Neurology. 2017;89:927–35.
4. Vance JM. Hereditary motor and sensory neuropathies. J Med Genet. 1991;28:1–5.
5. Suter U, Snipes GJ. Biology and genetics of hereditary motor and sensory neuropathies. Annu Rev Neurosci. 1995;18:45–75.
6. Harding AE. From the syndrome of Charcot, Marie and Tooth to disorders of peripheral myelin proteins. Brain. 1995;118(Pt 3):809–18.
7. Bergoffen J, Scherer SS, Wang S, Scott MO, Bone LJ, Paul DL, Chen K, Lensch MW, Chance PF, Fischbeck KH. Connexin mutations in X-linked Charcot-Marie-Tooth disease. Science. 1993;262:2039–42.
8. Bortolozzi M. What's the function of connexin 32 in the peripheral nervous system? Front Mol Neurosci. 2018;11:227.
9. Jagielnicki M, Kucharska I, Bennett BC, Harris AL, Yeager M. Connexin gap junction channels and hemichannels: insights from high-resolution structures. Biology (Basel). 2024;13:298.
10. Giaume C, Naus CC, Saez JC, Leybaert L. Glial connexins and pannexins in the healthy and diseased brain. Physiol Rev. 2021;101:93–145.
11. Balice-Gordon RJ, Bone LJ, Scherer SS. Functional gap junctions in the schwann cell myelin sheath. J Cell Biol. 1998;142:1095–104.
12. Abrams CK, Freidin MM, Verselis VK, Bennett MV, Bargiello TA. Functional alterations in gap junction channels formed by mutant forms of connexin 32: evidence for loss of function as a pathogenic mechanism in the X-linked form of Charcot-Marie-Tooth disease. Brain Res. 2001;900:9–25.
13. Laird DW, Lampe PD. Cellular mechanisms of connexin-based inherited diseases. Trends Cell Biol. 2022;32:58–69.
14. Oh S, Ri Y, Bennett MV, Trexler EB, Verselis VK, Bargiello TA. Changes in permeability caused by connexin 32 mutations underlie X-linked Charcot-Marie-Tooth disease. Neuron. 1997;19:927–38.
15. LeBlanc AC, Windebank AJ, Poduslo JF. P0 gene expression in Schwann cells is modulated by an increase of cAMP which is dependent on the presence of axons. Brain Res Mol Brain Res. 1992;12:31–8.
16. Abrams CK, Bennett MV, Verselis VK, Bargiello TA. Voltage opens unopposed gap junction hemichannels formed by a connexin 32 mutant associated with X-linked Charcot-Marie-Tooth disease. Proc Natl Acad Sci U S A. 2002;99:3980–4.
17. Gomez-Hernandez JM, de Miguel M, Larrosa B, Gonzalez D, Barrio LC. Molecular basis of calcium regulation in connexin-32 hemichannels. Proc Natl Acad Sci U S A. 2003;100:16030–5.
18. Liang GS, de Miguel M, Gomez-Hernandez JM, Glass JD, Scherer SS, Mintz M, Barrio LC, Fischbeck KH. Severe neuropathy with leaky connexin32 hemichannels. Ann Neurol. 2005;57:749–54.
19. De Vuyst E, Decrock E, Cabooter L, Dubyak GR, Naus CC, Evans WH, Leybaert L. Intracellular calcium changes trigger connexin 32 hemichannel opening. EMBO J. 2006;25:34–44.
20. Bayraktar E, Lopez-Pigozzi D, Bortolozzi M. Calcium regulation of connexin hemichannels. Int J Mol Sci. 2024;25:6594.
21. Saez JC, Schalper KA, Retamal MA, Orellana JA, Shoji KF, Bennett MV. Cell membrane permeabilization via connexin hemichannels in living and dying cells. Exp Cell Res. 2010;316:2377–89.
22. Wang N, De Bock M, Decrock E, Bol M, Gadicherla A, Vinken M, Rogiers V, Bukauskas FF, Bultynck G, Leybaert L. Paracrine signaling through plasma membrane hemichannels. Biochim Biophys Acta. 2013;1828:35–50.
23. Cotrina ML, Lin JH, Alves-Rodrigues A, Liu S, Li J, Azmi-Ghadimi H, Kang J, Naus CC, Nedergaard M. Connexins regulate calcium signaling by controlling ATP release. Proc Natl Acad Sci U S A. 1998;95:15735–40.
24. Anselmi F, Hernandez VH, Crispino G, Seydel A, Ortolano S, Roper SD, Kessaris N, Richardson W, Rickheit G, Filippov MA, et al. ATP release through connexin hemichannels and gap junction transfer of second messengers propagate Ca2+ signals across the inner ear. Proc Natl Acad Sci U S A. 2008;105:18770–5.
25. Di Virgilio F, Vultaggio-Poma V, Falzoni S, Giuliani AL. Extracellular ATP: a powerful inflammatory mediator in the central nervous system. Neuropharmacology. 2023;224:109333.
26. Saez JC, Green C. Involvement of connexin hemichannels in the inflammatory response of chronic diseases. Int J Mol Sci. 2018;19:2469.
27. Guo A, Zhang H, Li H, Chiu A, Garcia-Rodriguez C, Lagos CF, Saez JC, Lau CG. Inhibition of connexin hemichannels alleviates neuroinflammation and hyperexcitability in temporal lobe epilepsy. Proc Natl Acad Sci U S A. 2022;119:e2213162119.
28. Peng B, Xu C, Wang S, Zhang Y, Li W. The role of connexin hemichannels in inflammatory diseases. Biology (Basel). 2022;11:237.
29. Olympiou M, Sargiannidou I, Markoullis K, Karaiskos C, Kagiava A, Kyriakoudi S, Abrams CK, Kleopa KA. Systemic inflammation disrupts oligodendrocyte gap junctions and induces ER stress in a model of CNS manifestations of X-linked Charcot-Marie-Tooth disease. Acta Neuropathol Commun. 2016;4:95.
30. Xu L, Carrer A, Zonta F, Qu Z, Ma P, Li S, Ceriani F, Buratto D, Crispino G, Zorzi V, et al. Design and characterization of a human monoclonal antibody that modulates mutant connexin 26 hemichannels implicated in deafness and skin disorders. Front Mol Neurosci. 2017;10:298.
31. Ziraldo G, Buratto D, Kuang Y, Xu L, Carrer A, Nardin C, Chiani F, Salvatore AM, Paludetti G, Lerner RA, et al. A human-derived monoclonal antibody targeting extracellular connexin domain selectively modulates hemichannel function. Front Physiol. 2019;10:392.
32. Kuang Y, Zorzi V, Buratto D, Ziraldo G, Mazzarda F, Peres C, Nardin C, Salvatore AM, Chiani F, Scavizzi F, et al. A potent antagonist antibody targeting connexin hemichannels alleviates Clouston syndrome symptoms in mutant mice. EBioMedicine. 2020;57:102825.
33. Nardin C, Tettey-Matey A, Donati V, Marazziti D, Di Pietro C, Peres C, Raspa M, Zonta F, Yang G, Gorelik M, et al. A quantitative assay for Ca2+ uptake through normal and pathological hemichannels. Int J Mol Sci. 2022;23:7337.
34. Peres C, Sellitto C, Nardin C, Putti S, Orsini T, Di Pietro C, Marazziti D, Vitiello A, Calistri A, Rigamonti M, et al. Antibody gene transfer treatment drastically improves epidermal pathology in a keratitis ichthyosis deafness syndrome model using male mice. eBioMedicine. 2023;89:104453.
35. Chen TW, Wardill TJ, Sun Y, Pulver SR, Renninger SL, Baohan A, Schreiter ER, Kerr RA, Orger MB, Jayaraman V, et al. Ultrasensitive fluorescent proteins for imaging neuronal activity. Nature. 2013;499:295–300.
36. Tettey-Matey A, Di Pietro C, Donati V, Mammano F, Marazziti D. Generation of connexin-expressing stable cell pools. Methods Mol Biol. 2024;2801:147–76.

37. Gossen M, Bujard H. Tight control of gene expression in mammalian cells by tetracycline-responsive promoters. Proc Natl Acad Sci U S A. 1992;89:5547–51.

38. Cribbs AP, Kennedy A, Gregory B, Brennan FM. Simplified production and concentration of lentiviral vectors to achieve high transduction in primary human T cells. BMC Biotechnol. 2013;13:98.

39. Livak KJ, Schmittgen TD. Analysis of relative gene expression data using real-time quantitative PCR and the 2(-Delta Delta C(T)) Method. Methods. 2001;25:402–8.

40. Ceriani F, Ciubotaru CD, Bortolozzi M, Mammano F. Design and construction of a cost-effective spinning disk system for live imaging of inner ear tissue. Methods Mol Biol. 2016;1427:223–41.

41. Mammano F, Bortolozzi M. Ca2+ imaging: principles of analysis and enhancement. In: Verkhratsky A, Petersen O, editors. Calcium measurement methods, volume 43. New York: Humana Press; 2010. p. 57–80. [Wolf W (Series Editor): Neuromethods].

42. Morgan AJ, Jacob R. Ionomycin enhances Ca2+ influx by stimulating store-regulated cation entry and not by a direct action at the plasma membrane. Biochem J. 1994;300(Pt 3):665–72.

43. Pachitariu M, Stringer C, Dipoppa M, Schröder S, Rossi LF, Dalgleish H, Carandini M, Harris KD. Suite2p: beyond 10,000 neurons with standard two-photon microscopy. bioRxiv. 2017:061507. https://doi.org/10.1101/061507.

44. Li H, Liu TF, Lazrak A, Peracchia C, Goldberg GS, Lampe PD, Johnson RG. Properties and regulation of gap junctional hemichannels in the plasma membranes of cultured cells. J Cell Biol. 1996;134:1019–30.

45. Sanchez HA, Orellana JA, Verselis VK, Saez JC. Metabolic inhibition increases activity of connexin-32 hemichannels permeable to Ca2+ in transfected HeLa cells. Am J Physiol Cell Physiol. 2009;297:C665-678.

46. Qi C, Lavriha P, Bayraktar E, Vaithia A, Schuster D, Pannella M, Sala V, Picotti P, Bortolozzi M, Korkhov VM. Structures of wild-type and selected CMT1X mutant connexin 32 gap junction channels and hemichannels. Sci Adv. 2023;9:eadh4890.

47. Webb B, Sali A. Comparative protein structure modeling using MODELLER. Curr Protoc Protein Sci. 2016;86:2.9.1-2.9.37.

48. Nielsen BS, Zonta F, Farkas T, Litman T, Nielsen MS, MacAulay N. Structural determinants underlying permeant discrimination of the Cx43 hemichannel. J Biol Chem. 2019;294:16789–803.

49. Mirdita M, Schutze K, Moriwaki Y, Heo L, Ovchinnikov S, Steinegger M. ColabFold: making protein folding accessible to all. Nat Methods. 2022;19:679–82.

50. Buratto D, Saxena A, Ji Q, Yang G, Pantano S, Zonta F. Rapid assessment of binding affinity of SARS-COV-2 spike protein to the human angiotensin-converting enzyme 2 receptor and to neutralizing biomolecules based on computer simulations. Front Immunol. 2021;12:730099.

51. Páll S, Zhmurov A, Bauer P, Abraham M, Lundborg M, Gray A, Hess B, Lindahl E. Heterogeneous parallelization and acceleration of molecular dynamics simulations in GROMACS. J Chem Phys. 2020;153:134110.

52. Klauda JB, Venable RM, Freites JA, O'Connor JW, Tobias DJ, Mondragon-Ramirez C, Vorobyov I, MacKerell AD Jr, Pastor RW. Update of the CHARMM all-atom additive force field for lipids: validation on six lipid types. J Phys Chem B. 2010;114:7830–43.

53. Darden T, York D, Pedersen L. Particle mesh Ewald: An N·log(N) method for Ewald sums in large systems. J Chem Phys. 1993;98:10089–92.

54. Bussi G, Donadio D, Parrinello M. Canonical sampling through velocity rescaling. J Chem Phys. 2007;126:014101.

55. Parrinello M, Rahman A. Polymorphic transitions in single crystals: a new molecular dynamics method. J Appl Phys. 1981;52:7182–90.

56. Jurrus E, Engel D, Star K, Monson K, Brandi J, Felberg LE, Brookes DH, Wilson L, Chen J, Liles K, et al. Improvements to the APBS biomolecular solvation software suite. Protein Sci. 2018;27:112–28.

57. Humphrey W, Dalke A, Schulten K. VMD: visual molecular dynamics. J Mol Graph. 1996;14(33–38):27–38.

58. Seeliger D, de Groot BL. Protein thermostability calculations using alchemical free energy simulations. Biophys J. 2010;98:2309–16.

59. Gapsys V, Michielssens S, Seeliger D, de Groot BL. pmx: automated protein structure and topology generation for alchemical perturbations. J Comput Chem. 2015;36:348–54.

60. Klimovich PV, Shirts MR, Mobley DL. Guidelines for the analysis of free energy calculations. J Comput Aided Mol Des. 2015;29:397–411.

61. Zhou H, Chan KC, Buratto D, Zhou R. The rigidity of a structural bridge on HLA-I binding groove explains its differential outcome in cancer immune response. Int J Biol Macromol. 2023;253:127199.

62. Elfgang C, Eckert R, Lichtenberg-Frate H, Butterweck A, Traub O, Klein RA, Hulser DF, Willecke K. Specific permeability and selective formation of gap junction channels in connexin-transfected HeLa cells. J Cell Biol. 1995;129:805–17.

63. Beltramello M, Bicego M, Piazza V, Ciubotaru CD, Mammano F, D'Andrea P. Permeability and gating properties of human connexins 26 and 30 expressed in HeLa cells. Biochem Biophys Res Commun. 2003;305:1024–33.

64. Beltramello M, Piazza V, Bukauskas FF, Pozzan T, Mammano F. Impaired permeability to Ins(1,4,5)P3 in a mutant connexin underlies recessive hereditary deafness. Nat Cell Biol. 2005;7:63–9.

65. Bukauskas FF, Kreuzberg MM, Rackauskas M, Bukauskiene A, Bennett MV, Verselis VK, Willecke K. Properties of mouse connexin 30.2 and human connexin 31.9 hemichannels: implications for atrioventricular conduction in the heart. Proc Natl Acad Sci U S A. 2006;103:9726–31.

66. Vargas AA, Cisterna BA, Saavedra-Leiva F, Urrutia C, Cea LA, Vielma AH, Gutierrez-Maldonado SE, Martin AJ, Pareja-Barrueto C, Escalona Y, et al. On biophysical properties and sensitivity to gap junction blockers of connexin 39 hemichannels expressed in HeLa cells. Front Physiol. 2017;8:38.

67. Belliveau DJ, Bani-Yaghoub M, McGirr B, Naus CCG, Rushlow WJ. Enhanced neurite outgrowth in PC12 cells mediated by connexin hemichannels and ATP. J Biol Chem. 2006;281:20920–31.

68. Choi EJ, Palacios-Prado N, Saez JC, Lee J. Identification of Cx45 as a major component of GJs in HeLa cells. Biomolecules. 2020;10:1389.

69. Retamal MA, Reyes EP, Garcia IE, Pinto B, Martinez AD, Gonzalez C. Diseases associated with leaky hemichannels. Front Cell Neurosci. 2015;9:267.

70. Retamal MA, Fernandez-Olivares A, Stehberg J. Over-activated hemichannels: a possible therapeutic target for human diseases. Biochim Biophys Acta Mol Basis Dis. 2021;1867:166232.

71. Agha-Mohammadi S, O'Malley M, Etemad A, Wang Z, Xiao X, Lotze MT. Second-generation tetracycline-regulatable promoter: repositioned tet operator elements optimize transactivator synergy while shorter minimal promoter offers tight basal leakiness. J Gene Med. 2004;6:817–28.

72. Nagy JI, Ionescu AV, Lynn BD, Rash JE. Connexin29 and connexin32 at oligodendrocyte and astrocyte gap junctions and in myelin of the mouse central nervous system. J Comp Neurol. 2003;464:356–70.

73. Abrams CK, Goman M, Wong S, Scherer SS, Kleopa KA, Peinado A, Freidin MM. Loss of coupling distinguishes GJB1 mutations associated with CNS manifestations of CMT1X from those without CNS manifestations. Sci Rep. 2017;7:40166.

74. Sneyd J, Han JM, Wang L, Chen J, Yang X, Tanimura A, Sanderson MJ, Kirk V, Yule DI. On the dynamical structure of calcium oscillations. Proc Natl Acad Sci U S A. 2017;114:1456–61.

75. Nardin C, Mammano F. Measurement of Ca2+ uptake through connexin hemichannels. In: Mammano F, Retamal M, editors. Connexin hemichannels: methods and protocols. New York: Springer US; 2024. p. 97–109

76. Carrer A, Leparulo A, Crispino G, Ciubotaru CD, Marin O, Zonta F, Bortolozzi M. Cx32 hemichannel opening by cytosolic Ca2+ is inhibited by the R220X mutation that causes Charcot-Marie-Tooth disease. Hum Mol Genet. 2018;27:80–94.

77. Willebrords J, Maes M, Crespo Yanguas S, Vinken M. Inhibitors of connexin and pannexin channels as potential therapeutics. Pharmacol Ther. 2017;180:144–60.

78. Kapuscinski J. DAPI: a DNA-specific fluorescent probe. Biotech Histochem. 1995;70:220–33.

79. Orellana JA, Diaz E, Schalper KA, Vargas AA, Bennett MV, Saez JC. Cation permeation through connexin 43 hemichannels is cooperative, competitive and saturable with parameters depending on the permeant species. Biochem Biophys Res Commun. 2011;409:603–9.

80. Sáez JC, Vargas AA, Hernández DE, Ortiz FC, Giaume C, Orellana JA. Permeation of molecules through astroglial connexin 43 hemichannels is modulated by cytokines with parameters depending on the permeant species. Int J Mol Sci. 2020;21:3970.

81. Eskandari S, Zampighi GA, Leung DW, Wright EM, Loo DD. Inhibition of gap junction hemichannels by chloride channel blockers. J Membr Biol. 2002;185:93–102.

82. Buratto D, Wan Y, Shi X, Yang G, Zonta F. In silico maturation of a nanomolar antibody against the human CXCR2. Biomolecules. 2022;12:1285.

83. Wang L, Friesner RA, Berne BJ. Replica exchange with solute scaling: a more efficient version of Replica Exchange with Solute Tempering (REST2). J Phys Chem B. 2011;115:9431–8.

84. Almlof M, Aqvist J, Smalas AO, Brandsdal BO. Probing the effect of point mutations at protein-protein interfaces with free energy calculations. Biophys J. 2006;90:433–42.

85. Mammano F, Paller AS, White TW. Connexin hemichannel inhibition and human genodermatoses. J Investig Dermatol. S0022–202X(24)02053–0. https://doi.org/10.1016/j.jid.2024.08.003. Online ahead of print.

86. Buratto D, Donati V, Zonta F, Mammano F. Harnessing the therapeutic potential of antibodies targeting connexin hemichannels. Biochim Biophys Acta Mol Basis Dis. 2021;1867:166047.

87. Kaur S, Zhang X, Patel S, Rodriguez YA, Luther KJ, Alghafli G, Lang RM, Abrams CK, Dobrowsky RT. Pharmacologic targeting of the C-terminus of heat shock protein 90 improves neuromuscular function in animal models of Charcot Marie Tooth X1 disease. ACS Pharmacol Transl Sci. 2023;6:306–19.

88. Abrams CK, Lancaster E, Li JJ, Dungan G, Gong D, Scherer SS, Freidin MM. Knock-in mouse models for CMTX1 show a loss of function phenotype in the peripheral nervous system. Exp Neurol. 2023;360:114277.

89. Kim J, McFee M, Fang Q, Abdin O, Kim PM. Computational and artificial intelligence-based methods for antibody development. Trends Pharmacol Sci. 2023;44:175–89.

90. Lu R-M, Hwang Y-C, Liu IJ, Lee C-C, Tsai H-Z, Li H-J, Wu H-C. Development of therapeutic antibodies for the treatment of diseases. J Biomed Sci. 2020;27:1.

91. Chen X, Ravindra Kumar S, Adams CD, Yang D, Wang T, Wolfe DA, Arokiaraj CM, Ngo V, Campos LJ, Griffiths JA, et al. Engineered AAVs for non-invasive gene delivery to rodent and non-human primate nervous systems. Neuron. 2022;110:2242-2257 e2246.

92. Pisciotta C, Pareyson D. Gene therapy and other novel treatment approaches for Charcot-Marie-Tooth disease. Neuromuscul Disord. 2023;33:627–35.

93. Brown SDM. Advances in mouse genetics for the study of human disease. Hum Mol Genet. 2021;30:R274–84.

Publisher's Note